Available online at www.sciencedirect.com
SCIENCE DIRECT®
Journal of Computational Physics 213 (2006) 288–310
JOURNAL OF COMPUTATIONAL PHYSICS
www.elsevier.com/locate/jcp

Multiscale simulation of transport in an open quantum system: Resonances and WKB interpolation

Naoufel Ben Abdallah *, Olivier Pinaud

MIP, Laboratoire CNRS (UMR 5640), Université Paul Sabatier, 118, route de Narbonne, 31062 Toulouse Cedex 04, France

Received 7 October 2004; received in revised form 2 June 2005; accepted 15 August 2005
Available online 7 October 2005

Abstract

A numerical scheme for the one-dimensional stationary Schrödinger–Poisson model is described. The scheme is used to simulate a resonant tunneling diode and provides an important reduction of the simulation time. The improvement is two-fold. First the grid spacing in the position variable is made coarser by using oscillating interpolation functions derived from the WKB asymptotics. Then the discretization of the energy variable, which is a parameter for the Schrödinger equation, is improved by approaching the wavefunctions in the double barrier region by its projection on the resonant states (following the work of Presilla–Sjöstrand and Jona-Lasinio [On Schrödinger equations with concentrated non-linearities, Ann. Phys. 240 (1995) 1–21]).

MSC: 65P05; 77A99

Keywords: Schrödinger equation; Numerical scheme; Resonant tunneling diode; WKB approximation; Resonant states

1. Introduction

Over the last years, a wide variety of nanoscale semiconductor structures have been studied both experimentally and theoretically, for their potential application to ultrafast, low consumption and high functionality devices [19,22,45]. In such devices and at such lengthscales, quantum effects arize and have to be taken into account in the modelling by means of the Schrödinger equation. The oscillatory behaviour of the solutions of such an equation induces serious numerical difficulties and various strategies have been recently developed to reduce the correponding simulation times: reducing the spatial domain of the Schrödinger equation either by defining artificial boundary conditions [3–5,10] or by coupling the Schrödinger equation to classical models [9,11,13,20] or increasing the time step by using spectral type methods [7,8]. The large number of Schrödinger equations to be solved in order to simulate an electronic device as well as the difference of the lengthscales associated to each of them is another difficulty to be tackled to optimize the simulation codes.

* Corresponding author.
E-mail addresses: naoufel@mip.ups-tlse.fr (N.B. Abdallah), pinaud@mip.ups-tlse.fr (O. Pinaud).

0021-9991/$ - see front matter © 2005 Published by Elsevier Inc.
doi:10.1016/j.jcp.2005.08.012

Indeed, an electronic device is by essence an open system: electrons are injected from a reservoir (the source), they travel through the active region (channel of a Mosfet, double barrier of a resonant tunneling diode, etc.) and leave the device towards another reservoir (drain) [24,28,45]. In the reservoirs, scattering phenomena drive the electron ensemble towards a thermal equilibrium so that electrons are in a mixed state with the equilibrium statistics of the reservoir. Therefore, macroscopic quantities such as particle density or current density are computed as an integral over the energy variable of single state quantities [12,14,17,27,31–33,43].

Numerically, the integral is computed thanks to a suitable numerical integration method. An energy grid containing a certain amount of points is constructed and the wavefunction for each of these points is computed by solving the Schrödinger equation [17,27,18,22,41,43,37,39,44,42,29]. Depending on the features of the device (induced by geometry, lengthscales, resonances, etc.), a refined energy grid might be required for the simulation to be accurate enough. For instance, a resonant tunneling diode (RTD), which is our benchmark in this paper, behaves like a very precise energy filter; electrons having an energy extremely close to the resonant energy are transmitted from the source to the drain whereas the others are totally reflected back to the source. The transmission coefficient of the structure, as a function of the energy, has a very sharp peak at the resonant energy [20,36]. The width and the shape of this peak is of primary importance for computing the current flowing in the RTD since only transmitted electrons contribute to it. Therefore, a very refined mesh is needed around such energies resulting in a high computational cost. Consequently, an adequate treatment of resonances would help reducing the number of energy grid points and thus lowering the simulation time.

A second way to reduce the numerical burden is to allow for coarser space grids for the Schrödinger equation. For an RTD, and the situation is similar for other devices, the macroscopic quantities like particle density are relatively smooth functions of the position variable. As mentioned above, they are obtained as the sum of single state contributions. For high energies, the single states have a small de Broglie length and oscillate at much smaller space scale. Using the same spatial grid for all the energies to solve the Schrödinger equations with standard finite element or finite difference methods requires a large number of points and therefore increases unnecessarily the numerical cost.

The aim of this paper is to propose a method to reduce the simulation time for an RTD by both reducing the number of energy and position grid points. Before going into the details, let us recall the mathematical model to be solved [14].

1.1. The Schrödinger–Poisson problem

The RTD extends on the interval $[a,b]$ which contains the double barriers, the eventual spacers (region I in Fig. 1) and a small part of highly doped access regions (region II in Fig. 1). The transport is assumed to be ballistic and one-dimensional. The electrostatic potential is assumed to be constant outside the interval $[a,b]$, equal to V_a at the source contact a and to V_b at the drain contact b. The contacts a, b are linked to electron reservoirs at thermal equilibrium, injecting electrons with some given profiles $g_a(p)$, $p \geqslant 0$, $g_b(p)$, $p \leqslant 0$, where p is the momentum of the injected electron. The wave function of the electrons injected at $x = a$ with momentum $p \geqslant 0$ satisfies a stationary effective-mass Schrödinger equation with open boundary conditions:

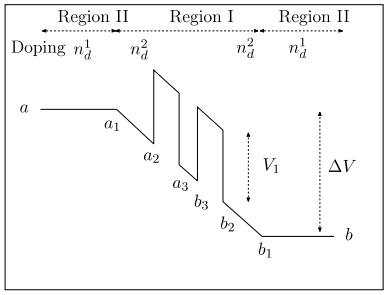

Fig. 1. Schematics of the potential energy in an RTD.

$$\begin{aligned} &-\frac{\hbar^2}{2m}\varphi_p'' - qV\varphi_p = E_p^a\varphi_p \quad (p \geqslant 0),\\ &\hbar\varphi_p'(a) + \mathrm{i}p\varphi_p(a) = 2\mathrm{i}p, \quad \hbar\varphi_p'(b) = \mathrm{i}p_b\varphi_p(b), \end{aligned} \tag{1}$$

where m and q are, respectively, the effective mass (assumed to be constant in the device) and the elementary (positive) charge of the electron, V is the total electrostatic potential in the device and

$$p_b = \sqrt{p^2 + 2qm(V_b - V_a)}, \quad E_p^a = \frac{p^2}{2m} - qV_a.$$

Similarly, electrons injected at $x = b$ with momentum $p \leqslant 0$ are represented by the wavefunction φ_p satisfying the equation,

$$\begin{aligned} &-\frac{\hbar^2}{2m}\varphi_p'' - qV\varphi_p = E_p^b\varphi_p \quad (p \leqslant 0),\\ &\hbar\varphi_p'(b) + \mathrm{i}p\varphi_p(b) = 2\mathrm{i}p, \quad \hbar\varphi_p'(a) = \mathrm{i}p_a\varphi_p(a), \end{aligned} \tag{2}$$

where

$$E_p^b = \frac{p^2}{2m} - qV_b, \quad p_a = \sqrt{p^2 + 2qm(V_a - V_b)}.$$

The transmission coefficients are defined by

$$T(p) = \frac{\sqrt{(p^2 + 2qm(V_b - V_a))^+}}{|p|}|\varphi_p(b)|^2 \quad \text{for } p > 0, \tag{3}$$

$$T(p) = \frac{\sqrt{(p^2 - 2qm(V_b - V_a))^+}}{|p|}|\varphi_p(a)|^2 \quad \text{for } p < 0, \tag{4}$$

where $(a)^+ = \max(a, 0)$. The electrons are assumed to be in a mixed state so that the electronic and current densities are given by

$$n(x) = \int_{-\infty}^{+\infty} g(p)|\varphi_p(x)|^2 \,\mathrm{d}p, \tag{5}$$

$$J = \frac{e}{m}\int_{-\infty}^{+\infty} g(p)pT(p) \,\mathrm{d}p, \tag{6}$$

where $g(p) := g_a(p)$ for $p > 0$, $g(p) := g_b(p)$, for $p < 0$ (g_a being the statistics of the electrons injected at $x = a$). Typically, $g(p)$ is a Fermi–Dirac integral given by

$$g(p) = \frac{mk_bT}{2\pi^2}\log\left(1 + \exp\left(\left(-\frac{p^2}{2m} + E_F\right)\Big/ k_bT\right)\right). \tag{7}$$

The electrostatic potential V is split into two parts: $V = V_\mathrm{e} + V_\mathrm{s}$, where V_e is the external potential (including double barriers, applied voltage) and V_s is the self-consistent potential modeling the electron–electron interaction and satisfies the Poisson equation

$$\begin{aligned} &\frac{\mathrm{d}^2V_\mathrm{s}}{\mathrm{d}x^2}(x) = \frac{q}{\varepsilon}(n(x) - n_\mathrm{D}(x)),\\ &V_\mathrm{s}(a) = V_\mathrm{s}(b) = 0, \end{aligned} \tag{8}$$

where ε is the dielectric constant and n_D the doping density.

1.2. Reducing the number of spatial grid points

The first difficulty is related to the Schrödinger equation resolution. In Fig. 2, it can be clearly observed that the electronic density varies rather smoothly. On the other hand, a single wavefunction strongly

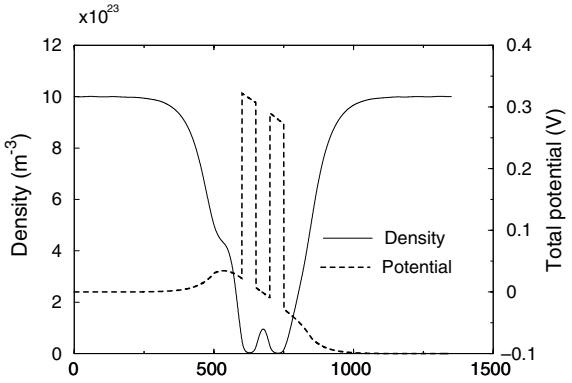

Fig. 2. Density profile in an RTD: smooth variation.

oscillates and the frequency depends on the electron energy, see Fig. 3. Consequently, even if the density seems not to require a refined grid, a small meshsize is needed in order to compute accurately the high energy wavefunctions.

In order to reduce the number of grid points, we notice that high energy wavefunctions correspond to a semiclassical regime. The need for a refined spatial grid is due to the linear or polynomial interpolation underlying the standard finite difference or finite element methods. Therefore, if the oscillation phase is known accurately, the phase factor could be used to interpolate the nodal values of the wave function and a coarser grid can be allowed. In the one-dimensional case, this can be done since the WKB asymptotics [16] provide us with an explicit formula for this phase factor. Let us mention that in the case of constant potentials, the WKB approach consists in using plane waves as interpolation functions. The idea has been developed by Ando and Itoh [1], and for the high frequency Helmholtz equation by Abboud et al. [2] (see also [21]). At the time being, the WKB method is restricted to the one-dimensional case. In two dimensions, the extension of the methods requires the construction of oscillating wave functions on a triangle which are approximate solutions of the Schrödinger equation. Simple computations for linear potentials show that the trace of some of these oscillating functions on one edge of the triangle does depend on the value of the function on the opposite vertex. The globally constructed function on the whold grid, will then have discontinuities on the edges which induces some difficulties in the definition of a related finite element scheme. Let us also mention that in two-dimensional applications like the double gate Mosfet (DGMOS) where there is a direction for transport and a direction for confinement, the two-dimensional Schrödinger equation is well approached by a one-dimensional non-diagonal Schrödinger system [38] for which a WKB type approach can be derived (see [15]).

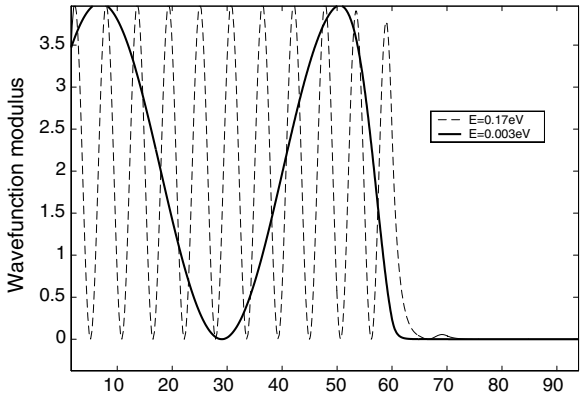

Fig. 3. A low energy (slowly varying) and a high energy (strongly oscillating) wave functions.

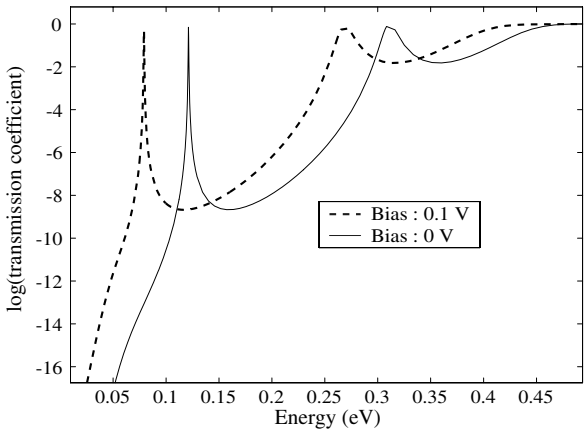

Fig. 4. Transmission coefficient for an RTD at two different biases.

1.3. Reducing the number of energy grid points

As can be seen in Fig. 4, the double barrier transmission coefficient presents a very sharp resonance peak with a very small resonance width, even in logarithmic scale. In [36], an automatic resonance detection method was used and showed fine results. Nevertheless, for time-dependent problems, since the resonances move (see Fig. 4), this method is not well suited and introduces an extra numerical cost. In order to deal with this problem, we define a new method to compute the density by adapting an idea developed by Presilla, Sjöstrand and Jona-Lasinio (the one-mode approximation [26,40]) which first consists in splitting the wavefunction into an exterior and an interior wavefunction. The exterior one is obtained by solving a modified Schrödinger equation in which the well inside the double barrier is ''filled''. The interior wave function essentially lives in the well between the two barriers. It is well approximated by its projection on the resonant states. In their paper [40], Presilla and Sjöstrand proceed to the exterior–interior decomposition of the wave function, they approximate the exterior function by its WKB approximation, project the interior on the resonant states and derive a differential equation on the proportionality coefficient between the interior solution and the resonant state. By doing so, they reduce the whole Schrödinger system to a finite dimensional differential equation. Of course, the model obtained by Presilla and Sjöstrand is an asymptotic model (see the thesis of Patel for a rigorous proof [35]). Our goal here is to extract from the approach a numerical scheme for the whole Schrödinger system. The key idea consists in noticing that the exterior solution does not exhibit any resonance. Therefore, its dependence with respect to energy is very smooth and does not require a refined energy grid. Now for the interior part, we still need a refined energy grid. But the gain here is the reduction to a finite number of unknowns (this number being equal to one in the targeted application).

1.4. Outline of the paper

The paper is organized as follows: in Section 2, we explain the WKB approach for the resolution of the Schrödinger equation while Section 3 is devoted to the treatment of the energy variable by the Presilla–Sjöstrand decomposition. Numerical results and comparisons are then given in Section 4. The expression of some coefficients of the scheme are given in Appendixes A and B.

2. The WKB-scheme

This section deals with the spatial discretization of the Schrödinger. Consider the following 1D Schrödinger problem, on the domain $[a, b]$,

$$-\frac{\hbar^2}{2m}\varphi''(x) + V(x)\varphi(x) = E\varphi(x), \tag{9}$$

$$\varphi(a) = \varphi_a, \quad \varphi'(a) = \varphi'_a, \tag{10}$$

where $\hbar$ is the reduced Planck constant, m is the particle mass, V a given potential and E a given energy. One has to notice here that the boundary conditions written above can be linked to that of (1) and (2) after easy manipulations (see [36] for more details). The problem (9) and (10) can be written as a first order ordinary differential problem

$$\Psi = \begin{pmatrix} \varphi \\ \varphi' \end{pmatrix}, \quad \Psi' = \begin{pmatrix} 0 & 1 \\ \frac{2m}{\hbar^2}(V-E) & 0 \end{pmatrix}\Psi, \quad \Psi(0) = \begin{pmatrix} \varphi_a \\ \varphi'_a \end{pmatrix}. \tag{11}$$

The system (11) can be solved using any numerical scheme like, for instance, the Runge–Kutta method. The meshsize has of course to be small enough in order to resolve the oscillations of the wave function φ. If λ is the de Broglie wavelength of the particle and if Δx is the meshsize, one needs

$$\frac{\Delta x}{\lambda} \ll 1.$$

For $\frac{\Delta x}{\lambda} \gg 1$, of course, the standard schemes fail. For a given Δx, this actually happens for sufficiently high energy wavefunctions. But the high energy regime is the semiclassical one. Therefore, the WKB asymptotics (see [16]) are valid. This leads, for $E > V(x)$, to the identities

$$\varphi(x) \sim_{\hbar\to 0} \frac{A}{\sqrt[4]{2m(E-V(x))}} e^{iS(x)} + \frac{B}{\sqrt[4]{2m(E-V(x))}} e^{-iS(x)}, \tag{12}$$

where A and B are two constants and $S(x)$ is the dimensionless action,

$$S(x) = \frac{\sqrt{2m}}{\hbar}\int_{x_0}^{x} \sqrt{E-V(s)}\, ds$$

and x_0 is an integration constant. Formula (12) gives the asymptotic behaviour of the wavefunction as $\hbar$tends to zero (or E to infinity). This asymptotics has two advantages: it is a good approximation not only at high frequencies but also for slowly varying potentials. As shown in (12), the wave function is the sum of two terms, each of them being the product of an oscillatory function and a slowly varying one. There is an analogous formulation of (12) for $E < V(x)$, classically forbidden energies. For the asymptotic formula (12) to be accurate, one needs the relation

$$\frac{\hbar m|V'|}{[2m(E-V)]^{3/2}} \ll 1. \tag{13}$$

Therefore, the asymptotics breaks down close to turning points defined as the set

$$\mathscr{T} = \{x \in [a,b],\ E = V(x)\}.$$

Notice that when the potential V is constant, (12) is exact.

2.1. WKB-basis construction

Let $(x_n)_{0\leqslant n\leqslant N}$ be a subdivision of $[a,b]$ such that

$$x_0 = a < x_1 < \cdots < x_n < \cdots < x_{N-1} < x_N = b,$$

and let

$$\mathscr{I}_n = [x_n, x_{n+1}].$$

The potential V is assumed to be in the space $\mathbb{P}_1$ of affine functions, that is to say

$$V(x) = a_n + b_n x \quad \text{for } x \in \mathscr{I}_n. \tag{14}$$

Let us assume that the nodal values φ_n, φ_{n+1} of the wave function φ are known. Standard linear interpolation consists in approaching φ on the interval $\mathscr{I}_n$ by the affine function which coincides with φ at the nodes x_n, x_{n+1}. Of course, the accuracy of the method is directly connected to the variation of φ versus the size of the cell $\mathscr{I}_n$. In particular, if φ is a solution of (9) with a high energy, the linear interpolation gives inaccurate results on a coarse grid. In order to enhance the accuracy on a coarse grid, we consider the WKB approximation to construct a new interpolation function. More precisely, the WKB-interpolated function is given by

$$\tilde{\varphi}(x) = \frac{A_n}{\sqrt[4]{2m(E-V(x))}} e^{iS(x)} + \frac{B_n}{\sqrt[4]{2m(E-V(x))}} e^{-iS(x)}, \quad x \in \mathscr{I}_n.$$

The constants A_n and B_n are computed by solving to the following 2×2 system

$$\varphi_n = \tilde{\varphi}(x_n) := \frac{A_n}{\sqrt[4]{2m(E-V(x_n))}} e^{iS(x_n)} + \frac{B_n}{\sqrt[4]{2m(E-V(x_n))}} e^{-iS(x_n)},$$
$$\varphi_{n+1} = \tilde{\varphi}(x_{n+1}) := \frac{A_n}{\sqrt[4]{2m(E-V(x_{n+1}))}} e^{iS(x_{n+1})} + \frac{B_n}{\sqrt[4]{2m(E-V(x_{n+1}))}} e^{-iS(x_{n+1})}.$$

After some easy algebraic manipulations, it follows readily

$$\tilde{\varphi}(x) = \alpha_n(x) f_n(x) \varphi_n + \beta_n(x) f_{n+1}(x) \varphi_{n+1}, \quad x \in \mathscr{I}_n, \tag{15}$$

where α_n and β_n are the so-called WKB-basis functions given by

$$\alpha_n(x) = -\frac{\sin S_{n+1}(x)}{\sin \gamma_n}, \quad \beta_n(x) = \frac{\sin S_n(x)}{\sin \gamma_n} \tag{16}$$

with

$$S_n(x) = \frac{\sqrt{2m}}{\hbar} \int_{x_n}^{x} \sqrt[+]{E - V(s)}\, ds, \quad \gamma_n = \frac{\sqrt{2m}}{\hbar} \int_{x_n}^{x_{n+1}} \sqrt[+]{E - V(s)}\, ds$$

and f_n are amplitude factors given by

$$f_n(x) = \sqrt[4]{\frac{E - V(x_n)}{E - V(x)}}.$$

In the above relations, $\sqrt[+]{}$ denotes the complex square root with non-negative imaginary part. Since V is in $\mathbb{P}_1$, S_n and γ_n can be computed explicitly. The expressions are given in Appendix A. Since the functions α_n and β_n oscillate at a frequency close to that of the wavefunction, it will be seen in the numerical computations that this method allows to choose a wide meshsize and therefore to decrease the number of points in the grid. Note also that for the WKB-interpolation function to exists, the phase γ_n is required to be different of a multiple of π, otherwise $\sin\gamma_n = 0$. This is a non-resonance condition, that we shall assume all along the paper.

Remark 2.1. Assume for example that V is constant, $E > V$ and denote $\lambda = \frac{\hbar}{\sqrt{2m(E-V)}}$. Then,

$$\alpha_n(x) = \frac{\sin(x_{n+1} - x)/\lambda}{\sin(x_{n+1} - x_n)/\lambda}, \quad \beta_n(x) = \frac{\sin(x - x_n)/\lambda}{\sin(x_{n+1} - x_n)/\lambda}, \quad x \in \mathscr{I}_n.$$

In the limit of small meshsizes compared to the wavelength, i.e., $(x_{n+1} - x_n)/\lambda \ll 1$, we have the following asymptotic formulae for α_n and β_n

$$\alpha_n(x) \simeq \frac{x_{n+1} - x}{x_{n+1} - x_n}, \quad \beta_n(x) \simeq \frac{x - x_n}{x_{n+1} - x_n}$$

which are exactly the expressions of the $\mathbb{P}_1$ basis functions.

When $|E - V(x)|$ is locally too small, (13) is in general not satisfied. Hence, we define a threshold δ up to which (15) will be used. When $|E - V(x)| < \delta$, we distinguish two cases:

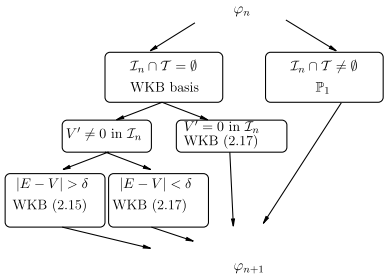

Fig. 5. Choices for the WKB-interpolation.

- $E - V$ has a constant sign in $\mathcal{I}_n$. In this case, we remove the singular prefactor $f_n(x)$ in the interpolation function and still keep the oscillating (or exponentially behaving) factors α_n and β_n. The wave function is then written under the form
$$\varphi(x) = \alpha_n(x)\varphi_n + \beta_n(x)\varphi_{n+1}, \quad x \in \mathcal{I}_n. \tag{17}$$
- When $E - V$ crosses zero in $\mathcal{I}_n$, a turning point, denoted by $\tilde{x}$, belongs to $\mathcal{I}_n$ and the WKB function are no longer suitable. In this case the Schrödinger equation implies $\varphi''(\tilde{x}) = 0$ and then φ is almost a linear function. Therefore, we use a $\mathbb{P}_1$ interpolation function φ
$$\varphi(x) = u_n(x)\varphi_n + v_n(x)\varphi_{n+1}, \quad x \in \mathcal{I}_n \tag{18}$$
with
$$u_n(x) = 1 - \frac{(x - x_n)}{(x_{n+1} - x_n)}, \quad v_n(x) = \frac{(x - x_n)}{(x_{n+1} - x_n)}.$$

2.2. Discretization of the Schrödinger equation

Eq. (9) is discretized using a finite volume approach: we integrate it between $x_{n+\frac{1}{2}}$ and $x_{n-\frac{1}{2}}$, where $x_{n\pm\frac{1}{2}} = \frac{1}{2}(x_n + x_{n\pm1})$, which leads to
$$\varphi'_{n+\frac{1}{2}} - \varphi'_{n-\frac{1}{2}} = -\frac{2m}{\hbar^2}\int_{x_{n-\frac{1}{2}}}^{x_{n+\frac{1}{2}}} (E - V(x))\varphi(x)\,\mathrm{d}x, \tag{19}$$
where $\varphi'_{n\pm\frac{1}{2}} = \varphi'(x_{n\pm\frac{1}{2}})$. Projecting φ on the different basis (15), (17) and (18) leads to the following three-point scheme for the Schrödinger equation
$$\varphi_{n+1} = \frac{1}{A_n}\left((B_n + \tilde{B}_{n-1})\varphi_n + \tilde{C}_{n-1}\varphi_{n-1}\right), \tag{20}$$
where the coefficients $A_n, B_n, \tilde{B}_{n-1}, \tilde{C}_{n-1}$ are computed exactly and are given in Appendix A. A_n and B_n are calculated at the step n while $\tilde{B}_{n-1}$ and $\tilde{C}_{n-1}$ at the step $n-1$. In the limit $\Delta x \ll \lambda$, the scheme boils down to the standard finite difference scheme for the Schrödinger equation. The different steps of the algorithm are summarized in Fig. 5.

3. The Presilla–Sjöstrand decomposition

We define in this section the numerical method allowing the reduction of energy grid points for an RTD. Such a device is obtained by stacking successive layers of different semiconductors (typically GaAs and GaAlAs). This results in an double barrier shaped electrostatic potential energy as shown in Fig. 1. The transmission coefficient presents sharp peaks at some energies called resonant energies and the double barrier is quasi opaque for energies different from these resonant energies.

Presilla, Sjöstrand and Jona-Lasinio [26,40] decomposition consists in splitting the wave function φ_p, solution of (1), into an exterior part, φ_p^{ext}, essentially localized outside the barriers and an interior one, φ_p^{int}, essentially localized in the well between the two barriers

$$\varphi_p = \varphi_p^{\text{ext}} + \varphi_p^{\text{int}}. \tag{21}$$

The exterior solution is defined as the solution of

$$\begin{aligned} &-\frac{\hbar^2}{2m}\frac{\mathrm{d}^2\varphi_p^{\text{ext}}}{\mathrm{d}x^2} - qV_{\text{fill}}\varphi_p^{\text{ext}} = E_p^a\varphi_p^{\text{ext}} \quad (p \geqslant 0),\\ &\hbar\frac{\mathrm{d}\varphi_p^{\text{ext}}}{\mathrm{d}x}(a) + \mathrm{i}p\varphi_p^{\text{ext}}(a) = 2\mathrm{i}p, \quad \hbar\frac{\mathrm{d}\varphi_p^{\text{ext}}}{\mathrm{d}x}(b) = \mathrm{i}p_b\varphi_p^{\text{ext}}(b), \end{aligned} \tag{22}$$

where V_{fill} is equal to the potential V with a filled well: the well between the two barriers is "filled" so that the whole zone is replaced by a single thick barrier (see Fig. 6). The interior solution is the solution of the non-homogeneous Schrödinger equation

$$\begin{aligned} &-\frac{\hbar^2}{2m}\frac{\mathrm{d}^2\varphi_p^{\text{int}}}{\mathrm{d}x^2} - qV\varphi_p^{\text{int}} = E_p^a\varphi_p^{\text{int}} + q(V_{\text{fill}} - V)\varphi_p^{\text{ext}} \quad (p \geqslant 0),\\ &\hbar\frac{\mathrm{d}\varphi_p^{\text{int}}}{\mathrm{d}x}(a) + \mathrm{i}p\varphi_p^{\text{int}}(a) = 0, \quad \hbar\frac{\mathrm{d}\varphi_p^{\text{int}}}{\mathrm{d}x}(b) = \mathrm{i}p_b\varphi_p^{\text{int}}(b). \end{aligned} \tag{23}$$

The source term in this equation is localized in the quantum well and has a non-zero contribution to φ_p^{int} when the energy E_p^a is close to resonant energies (see [6,30]) defined as the non-trivial solutions of the eigenvalue problem

$$-\frac{\hbar^2}{2m}e_\lambda''(x) - qV(x)e_\lambda(x) = \lambda e_\lambda(x), \tag{24}$$

$$\hbar e_\lambda'(a) + \mathrm{i}\sqrt[+]{2m(\lambda + qV_a)}e_\lambda(a) = 0, \quad \hbar e_\lambda'(b) = \mathrm{i}\sqrt[+]{2m(\lambda + qV_b)}e_\lambda(b), \tag{25}$$

where the eigenvalue $\lambda = E_R - i\Gamma/2$ has necessary a non-vanishing imaginary part. The eigenfunction e_λ is of class L^2 on the contour

$$\gamma := \left(\mathrm{e}^{\mathrm{i}\theta}]\infty, 0] + a_1\right) \cup [a_1, b_1] \cup \left(b_1 + \mathrm{e}^{\mathrm{i}\theta}[0, +\infty[\right)$$

for θ conveniently chosen and satisfies

$$\int_\gamma e_\lambda(x)^2\,\mathrm{d}x = 1, \quad \int_\gamma e_\lambda(x)e_\lambda'(x)\,\mathrm{d}x = 0.$$

The system (24) and (25) is a non-linear eigenvalue problem which can be solved, as explained later on, by a perturbative approach.

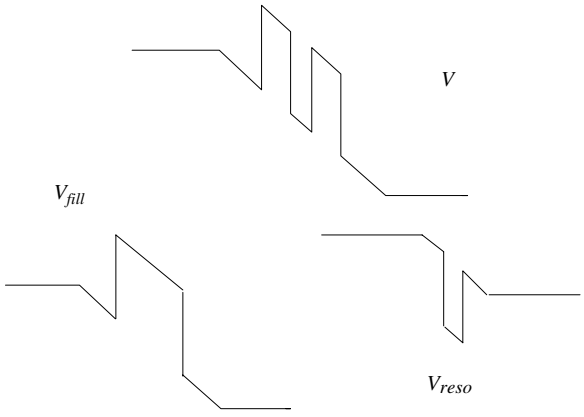

Fig. 6. "True", "Filled" and "Resonant" potential. The different potentials.

When the energy is close to one resonant energy, the source term in (23) produces a non-negligible contribution. The solution φ_p^{int} is then approximated by a linear combination of the resonant states. The details explaining why this approximation is accurate can be found in [40]. In the case of an RTD, only the ground resonant state is significantly populated. Indeed, for energies close to the second resonant energy, the statistics $g(p)$ (7) is very small, so that there is no contribution of these states to the density or current. Hence, higher resonant states are neglected and φ_p^{int} is assumed to be proportional to the ground state e. The proportionality coefficient, called the amplitude factor, depends quasi-explicitly on p. One advantage of this decomposition is that it allows a relatively large energy mesh for the computation of φ_p^{ext} since there is no resonance to resolve. On the other hand, the computation of φ_p^{int} for which a fine energy grid is required reduces to the computation of the amplitude factor which is much simpler to perform. In [40], the functions φ_p^{ext} and e are approximated by means of WKB expansions and a reduced model for the RTD is obtained with quasi-explicit formula. In this paper, we do not replace the wavefunctions by their WKB approximation but rather use this approximation to build an adequate numerical scheme. Let us mention that the rigorous mathematical justification of this method has been studied by Nier and Patel [34,35].

Computing the resonant states. If λ is a real number, then (24) and (25) admits no solutions except the vanishing one. Nevertheless, as soon as $\Gamma > 0$, (24) and (25) has several solutions. Let us define the self-adjoint operator $\mathscr{H} = -\mathrm{d}^2/\mathrm{d}x^2 - qV_{\text{reso}}$ defined on $[c,d]$, with $c \in [a_1,a_2]$, $d \in [b_2,b_1]$ equipped with Dirichlet boundary conditions at c and d and where the potential V_{reso} is defined by (see Fig. 6),

$$V_{\text{reso}} = \mathbf{1}\mathbf{I}_{[a_2,b_2]}V + \mathbf{1}\mathbf{I}_{[c,a_2]}V(a_2^+) + \mathbf{1}\mathbf{I}_{[b_2,d]}V(b_2^-).$$

The potential V_{reso} is nothing but the potential V with thicker barriers. The such defined operator $\mathscr{H}$ admits a purely discrete real spectrum. It is proven in particular by Nier and Patel, since e decays exponentially in the barriers, that e is close to the ground state of $\mathscr{H}$ and then the real part of the resonance E_{R} is very well approximated by the value of the first eigenenergy of $\mathscr{H}$. The ground state of $\mathscr{H}$ is denoted by $\tilde{e}$ and then solves

$$\begin{aligned} &\mathscr{H}\tilde{e} = \tilde{E}_{\text{R}}\tilde{e}, \\ &\tilde{e}(c) = \tilde{e}(d) = 0. \end{aligned} \tag{26}$$

The real part E_{R} of λ is approximated by $\tilde{E}_{\text{R}}$ and the value of e inside the well is approximated by $\tilde{e}$.

Following [40], the eigenstate $\tilde{e}$ can be now extended outside the double-barrier in order to recover an approximation of the full eigenstate e:

$$e(x,\Gamma) \approx \begin{cases} e_l(x,\Gamma) & \text{for } x \in [a,a_3], \\ \tilde{e}(x) & \text{for } x \in [a_3,b_3], \\ e_r(x,\Gamma) & \text{for } x \in [b_3,b], \end{cases}$$

where $e_l(x,\Gamma)$ and $e_g(x,\Gamma)$ are the left and right extended functions given by

$$\begin{aligned} &-\frac{\hbar^2}{2m}e_l'' - qVe_l'' = (E_{\text{R}} - i\Gamma/2)e_l \quad \text{on } [a,a_3], \\ &\hbar e_l'(a) + \mathrm{i}\sqrt[+]{2m(E_{\text{R}} - \mathrm{i}\Gamma/2 + qV_a)}e_l(a) = 0, \quad e_l(a_3) = \tilde{e}(a_3), \end{aligned} \tag{27}$$

$$\begin{aligned} &-\frac{\hbar^2}{2m}e_r'' - qVe_r'' = (E_{\text{R}} - \mathrm{i}\Gamma/2)e_r \quad \text{on } [b_3,b], \\ &\hbar e_r'(b) - \mathrm{i}\sqrt[+]{2m(E_{\text{R}} - i\Gamma/2 + qV_b)}e_r(b) = 0, \quad e_r(b_3) = \tilde{e}(b_3). \end{aligned} \tag{28}$$

The resonance width can now be computed thanks to (24): multiplying (24) by $\bar{e}$, integrating over $[a',b']$, where $a' < a_1$, $b' > b_1$ and taking the imaginary part leads to

$$\Gamma \int_{a'}^{b'} |e(x,\Gamma)|^2 \,\mathrm{d}x = \frac{\hbar^2}{m}\mathscr{I}m\left(\overline{e(x,\Gamma)}e'(x,\Gamma)\right)\Big|_{a'}^{b'}. \tag{29}$$

This last equation is non-linear since $e(x,\Gamma)$ depends on Γ through the boundary conditions of (27) and (28) and the Schrödinger equation. Solving numerically the fully non-linear problem induces extra-numerical cost and the final computational gain would not be as important as expected. Nevertheless, since in practice

$\Gamma/2E_R \ll 1$ (typically $\Gamma/2E_R = 1e-4$, this is why the resonance peak is sharp), it can be computed by an iteration argument. The value Γ_0 defined by

$$\Gamma_0 \int_{a'}^{b'} |e(x,0)|^2 \,\mathrm{d}x = \frac{\hbar^2}{m} \mathscr{I}m\Big(\overline{e(x,0)} e'(x,0)\Big)\Big|_{a'}^{b'}$$

is already a good estimate of Γ. Nevertheless, it is expected that the electronic density is a $\mathcal{O}(\Delta\Gamma^\alpha)$ with α close to one and where $\Delta\Gamma$ is the error made on Γ. Then, to obtain a refined guess, we iterate once more an write

$$\Gamma_1 \int_{a'}^{b'} |e(x,\Gamma_0)|^2 \,\mathrm{d}x = \frac{\hbar^2}{m} \mathscr{I}m\Big(\overline{e(x,\Gamma_0)} e'(x,\Gamma_0)\Big)\Big|_{a'}^{b'}.$$

The amplitude factor. We are able now to evaluate the wave function φ_p. The interior wave function φ_p^{int} solves (23), that we recall here

$$-\frac{\hbar^2}{2m}\frac{\mathrm{d}^2\varphi_p^{\mathrm{int}}}{\mathrm{d}x^2} - qV\varphi_p^{\mathrm{int}} = E_p^a \varphi_p^{\mathrm{int}} + q(V_{\mathrm{fill}} - V)\varphi_p^{\mathrm{ext}} \quad (p \geqslant 0).$$

Taking the scalar product of (23) with e leads to the final expression

$$\varphi_p^{\mathrm{int}} = \theta^a(p) e(x) \tag{30}$$

with

$$\theta^a(p) = \frac{1}{E_p^a - \lambda} \frac{q\int_{a_3}^{b_3} (V_{\mathrm{fill}} - V)\varphi_p^{\mathrm{ext}} \bar{e}(x)\,\mathrm{d}x}{\int_{a_3}^{b_3} |e(x)|^2 \,\mathrm{d}x}. \tag{31}$$

The fast variation of $\theta^a(p)$ near resonances is not induced by the integral $\int_{a_3}^{b_3} (V_{\mathrm{fill}} - V)\varphi_p^{\mathrm{ext}} \bar{e}(x)\,\mathrm{d}x$ which variation with respect to p only requires a coarse energy grid, but rather by the prefactor $1/(E_p^a - \lambda)$ which is responsible for the well known Lorenzian Shape of the resonance [16,22].

Remark 3.1. Notice that theoretically, following (1) and (22), φ_p^{int} solves

$$\hbar\frac{\mathrm{d}\varphi_p^{\mathrm{int}}}{\mathrm{d}x}(a) + \mathrm{i}p\varphi_p^{\mathrm{int}}(a) = 0, \quad \hbar\frac{\mathrm{d}\varphi_p^{\mathrm{int}}}{\mathrm{d}x}(b) = \mathrm{i}p_b\varphi_p^{\mathrm{int}}(b).$$

But, according to (30), φ_p^{int} verifies

$$\hbar\frac{\mathrm{d}\varphi_p^{\mathrm{int}}}{\mathrm{d}x}(a) + \mathrm{i}p\varphi_p^{\mathrm{int}}(a) = \mathrm{i}\Big(p - \sqrt[+]{2m(\lambda + qV_a)}\Big)\varphi_p^{\mathrm{int}}(a),$$
$$\hbar\frac{\mathrm{d}\varphi_p^{\mathrm{int}}}{\mathrm{d}x}(b) - \mathrm{i}p_b\varphi_p^{\mathrm{int}}(b) = -\mathrm{i}\Big(p_b - \sqrt[+]{(2m\lambda + qV_b)}\Big)\varphi_p^{\mathrm{int}}(b).$$

These conditions are equivalent in practice since the r.h.s. of the above equalities almost vanish for two reasons. First, neglecting Γ, if $p^2 \approx 2m(E_R + qV_a)$, then $p - \sqrt[+]{2m(E_R + qV_a)} \approx 0$ and $p_b - \sqrt[+]{2m(E_R + qV_b)} \approx 0$ and also if $p^2 \neq 2m(E_R + qV_a)$, then according to (30), φ_p^{int} is small. Second, since e decays exponentially in the barriers, it is expected that $e(a)$ and $e(b)$ are extremely small.

For p negative, we obtain analogously

$$-\frac{\hbar^2}{2m}\frac{\mathrm{d}^2\varphi_p^{\mathrm{ext}}}{\mathrm{d}x^2} - qV_{\mathrm{fill}}\varphi_p^{\mathrm{ext}} = E_p^b\varphi_p^{\mathrm{ext}} \quad (p \leqslant 0),$$
$$\hbar\frac{\mathrm{d}\varphi_p^{\mathrm{ext}}}{\mathrm{d}x}(b) + \mathrm{i}p\varphi_p^{\mathrm{ext}}(b) = 2\mathrm{i}p, \quad \hbar\frac{\mathrm{d}\varphi_p^{\mathrm{ext}}}{\mathrm{d}x}(a) = -\mathrm{i}p_a\varphi_p^{\mathrm{ext}}(a)$$

for the driving term and

$$\theta^b(p) = \frac{1}{E_p^b - \lambda} \frac{q\int_{a_3}^{b_3} (V_{\mathrm{fill}} - V)\varphi_p^{\mathrm{ext}} \bar{e}(x)\,\mathrm{d}x}{\int_{a_3}^{b_3} |e(x)|^2 \,\mathrm{d}x}, \quad \varphi_p^{\mathrm{int}} = \theta^b(p) e(x).$$

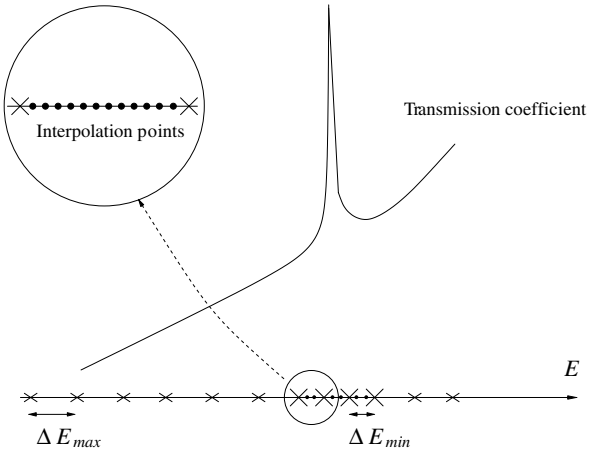

Fig. 7. The energy mesh.

3.1. Numerical procedure

The successive steps of the computation of the density n and their numerical resolution are summarized below.

All the potentials are discretized in the space $\mathbb{P}_1$ on a mesh $(x_n)_{0\leqslant n\leqslant N}$.

Operations independent of p

- *Step* 1: computation of E_{R} and $\tilde{e}$. Since the minimal meshsize of the mesh $(x_n)_{0\leqslant n\leqslant N}$ is relatively large, a multigrid method is used: the mesh is refined by dividing each cell by into equally sized N_{GR} cells. Eq. (26) is solved after a discretization of $\tilde{e}$ in $\mathbb{P}_1$ on the new mesh. This leads to a generalized eigenvalue problem solved with the inverse power method after a tridiagonal Househölder reduction [23].
- *Step* 2: computation of Γ and e. Eqs. (28) and (27) are solved using the WKB-scheme and then the solution are connected to $\tilde{e}$ in order to form e. Γ is calculated thanks to Eq. (29).

Operations depending on p

- *Step* 3: computation of φ_p^{ext}. The WKB-scheme is used to solve (22), see [36] for the treatment of the open boundary conditions.
- *Step* 4: computation of φ_p^{int}. $\theta(p)$ is calculated thanks to φ_p^{ext}, λ, e and Eq. (31).
- Final step : computation of n. n is given by formula (5). The integration with respect to p is performed with the following method. Let σ a given threshold. If $|p^2 - qV_a - E_R| > \sigma$, the energy meshsize is chosen to be equal to $\Delta E_{\max}$. On the other hand, if $|p^2 - qV_a - E_{\mathrm{R}}| < \sigma$, the meshsize is $\Delta E_{\min}$ (see Fig. 7). Contrary to the adaptative method used in [36], $\Delta E_{\max}$ is close to $\Delta\ E_{\min}$ and then the number of points in the grid is reduced. Nevertheless, in the domain $|p^2 - qV_a - E_{\mathrm{R}}| < \sigma$, one needs a very refined energy grid in order to compute $\theta^a(p)$ from (31). Hence, between two energy grid points, φ_p^{ext} is linearly interpolated with respect to p in N_{interp} points.

4. Numerical results

In this section, we show the efficiency of the approaches explained in Section 2 and 3, some numerical results illustrating the two methods are presented for the resonant tunneling diode. First, we concentrate on the WKB-scheme for linear Schrödinger equation. Second, the Presilla–Sjöstrand decomposition is tested in a

Table 1
RTD parameters

a	a_1	a_2	a_3	b_3	b_2	b_1	b	m_{eff}	V_1
0 nm	50 nm	60 nm	65 nm	70 nm	75 nm	85 nm	1350 nm	$0.067m_e$	−0.3 V

linear situation and then in the self-consistent case. All along the numerical investigations, the RTD has the parameters used in [36], see Table 1.

Within this section, RK refers to the fourth-order Runge–Kutta method. In order to compare precisely the various methods, the used mesh for RK is the same as the one used for WKB-scheme. Nevertheless, since RK needs more points to give accurate results, the RK spatial grid is obtained from the WKB grid by splitting each WKB cell into several equally sized small cells.

4.1. Validation of the WKB-scheme

The WKB-scheme efficiency is first evaluated in a simple case where analytic expressions are available. This case corresponds to a double-barrier heterostructure under a zero bias. In a second time, the scheme is tested on a double-barrier under a non-zero bias. An electrostatic potential is added in order to introduce turning points in the simulation. The WKB-scheme is always compared to RK. The value of the threshold δ is set at 0.08 eV.

4.1.1. A simple case

The problem (1) can be solved analytically assuming that no bias is applied to the structure (see Fig 1) with $\Delta V = 0$. Indeed, since in this case V is piecewise constant, the Schrödinger equation can be explicitly solved and the continuity of the wavefunction and its derivative define an 8×8 linear system. Two different energies are considered: one very close to the double-barrier first resonant energy and the other far from this value. The results are presented in Figs. 9 and 8.

At the resonant energy (Fig. 8), $E_p^a = 0.08958$ eV and the WKB mesh contains 13 points. The relative l^2 error at the nodal points between the exact solution and the one obtained thanks to the WKB-scheme is about 4×10^{-12}%. With a 15 times finer grid (193 nodes), the RK method has a computational cost 11 times higher than WKB and produces an l^2 error of the order of 2.5%. With a 10 times finer grid instead, the error rises to 11% with a computational cost 5 times greater than the WKB one.

For an energy $E_p^a = 0.046072$ eV (Fig. 9), the wavelength is larger and the efficiency is expected to be less important. In this case the WKB mesh contains 15 points and the relative node error is 2.2×10^{-13}%. For RK, on 5 times finer grid, the node error is 1.5% with a time cost only 3.3 times higher. With a 2 times finer grid, the error is 16% and the time cost is twice higher. The results are summarized in Table 2.

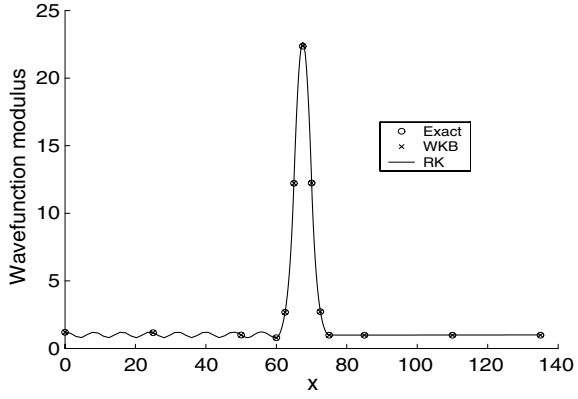

Fig. 8. Comparison Exact-WKB-RK: resonant case with 15 points added.

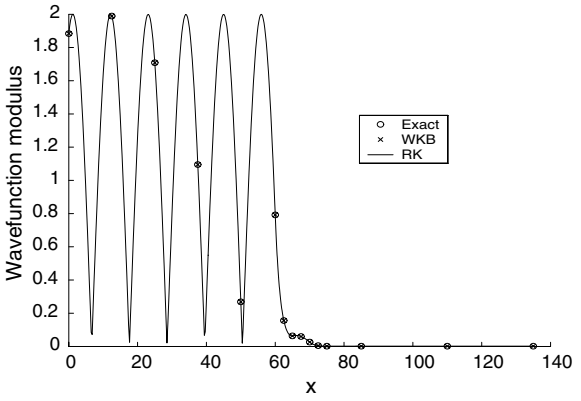

Fig. 9. Comparison Exact-WKB-RK: non-resonant case.

Table 2
Results for the linear case

	N	Error	Time	N	Error	Time
	$E = 0.08958$ eV			$E = 0.046072$ eV		
WKB	13	4×10^{-14}	1	15	2.2×10^{-15}	1
RK	133	0.11	5	45	0.16	2
	193	0.025	11	85	0.015	3.3

4.1.2. A case with turning points

A bias of 0.08 V is now applied at the edges of the device, and no explicit formula is provided for the solution. An electrostatic potential is added in order to introduce turning points in the simulation. This potential is actually the self-consistent potential obtained by coupling to the Poisson equation. As reference, the solution obtained thanks to RK with a mesh containing a very high number of points is taken (1024). This solution is then compared to WKB and RK with less points.

For a small energy of 0.0039 eV, the error is 0.64% for WKB on a 34 points grid. It is and 5e-3% for RK on a 6 times finer grid (232 points), see Fig. 10. RK simulation is twice longer than WKB with such parameters.

For a higher energy with E = 0.17 eV, and afterwards without turning points (Fig. 11), the WKB error is 0.1% while the RK error is 1.1 % with an 8 times finer grid (298 points). In this case, WKB is about 3 times faster. The results are summarized in Table 3.

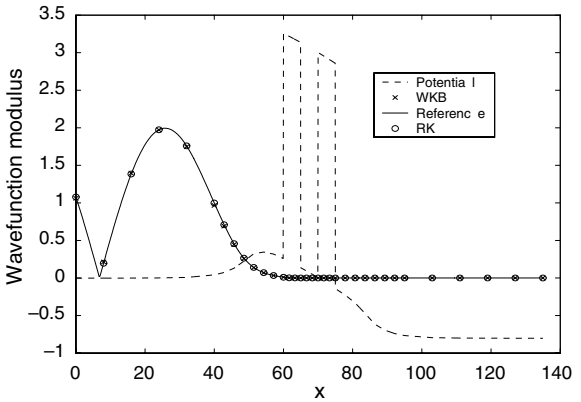

Fig. 10. Comparison Reference-WKB-RK: small energy case with turning points.

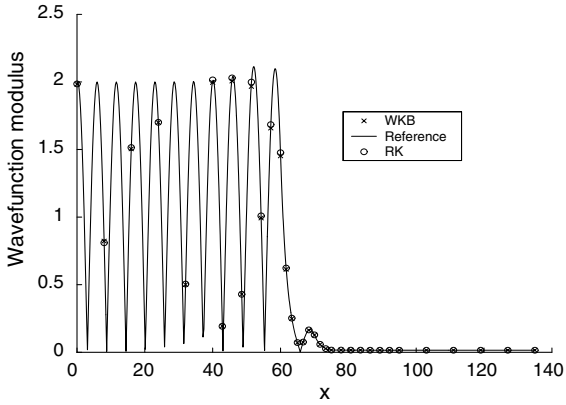

Fig. 11. Comparison Reference-WKB-RK: high energy case.

Table 3
Results for the linear case with turning points

	N	Error	Time	N	Error	Time
	$E = 0.0039$ eV			$E = 0.17$ eV		
WKB	34	0.0064	1	34	0.001	1
RK	232	5e − 5	2	298	0.011	3

For an energy of 0.059 eV, in order have a comparison with the reference solution, the wavefunction is evaluated at the reference mesh points thanks to the WKB basis functions. In Fig. 12, the reference and the WKB-interpolated function are almost undistinguishable and the global L^2 error between them is 1.6%.

The scheme was also tested in a physically non-relevant case with a very high energy in order to have a meshsize large compared to the wavelength. For an energy of 1.11 eV, the computed wavefunction is represented in Fig. 13 and the obtained error is about 0.81% compared to the same reference as above.

4.2. Validation of the one-mode approximation

In this section, the Presilla–Sjöstrand approach is illustrated on two examples. The first one corresponds to Section 4.1.1 where exact solutions are available. The second one is the fully non-linear RTD model. In both cases, the electronic density is computed thanks to (5) and after an integration between $-k_{\max}$ and $k_{\max}$. For

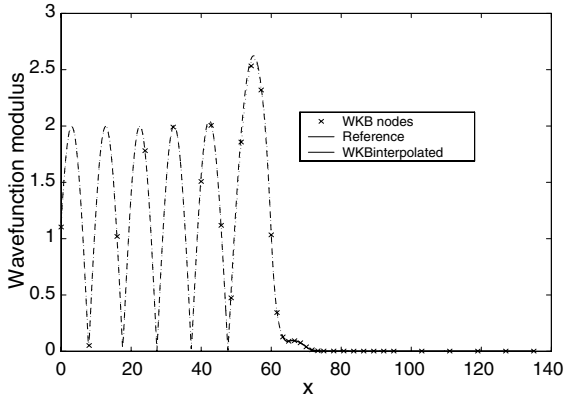

Fig. 12. WKB-Interpolated low energy wavefunction.

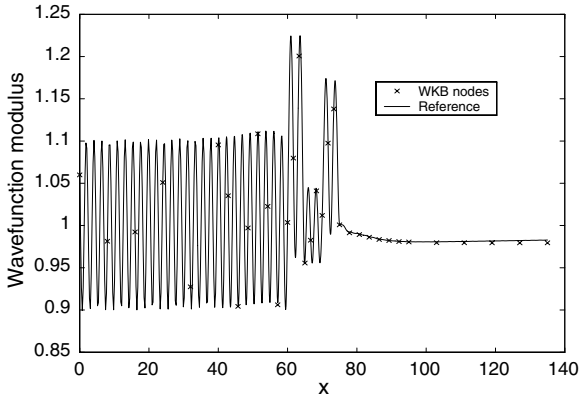

Fig. 13. WKB-Interpolated very high energy energy wavefunction.

convenience, the wave vector k (defined as $k = \sqrt{2mE}/\hbar$) is used instead of the energy E. The quantities $\Delta k_{\max}$, $\Delta k_{\min}$ and σ, respectively, denote the maximal, the minimal meshsize and the threshold for the one-mode approximation (see Section 3.1).

Both examples share the parameters presented in Table 4.

4.2.1. A linear case

We consider the configuration of Section 4.1.1 where exact solutions are provided. The exact expressions of the density is compared to the results given by the one-mode approximation and the method used in [36]. The latter consists in solving the Schrödinger equations for a both side injection with RK and in adaptating the energy meshsize thanks to the slope of the logarithm of the transmission coefficient. The results are presented in Figs. 14 and 15. The used grid contains 19 points for WKB and is 6 times finer for RK. For almost the same error 0.1 % and 0.12 %, RK is about 6 times longer.

Between two WKB grid points, the density can be computed either by linearly interpolating the nodal values, or by WKB-interpolating the wave functions and then superposing their contribution to reconstruct the density. The results are similar with a discrepancy of 0.1%.

In Fig. 16, the interior wave function, defined by $\varphi_p - \varphi_p^{\text{ext}}$, is represented for several energies close to the resonant one. It can be observed that the wave functions have globally the same shape modulated by an amplitude factor depending on the energy. To check more accurately the validity of the one-mode approximation, we have the quantity

$$Q = \frac{|\langle \varphi_p - \varphi_p^{\text{ext}}, e\rangle|}{\|\varphi_p - \varphi_p^{\text{ext}}\|_{L^2}\|e\|_{L^2}}$$

where $\langle\cdot,\cdot\rangle$ denotes the L^2 inner product. When Q is equal to one, this expresses that $\varphi_p - \varphi_p^{\text{ext}} = \theta(p)e(x)$ and thus one-mode approximation is exact. In Fig. 17, one can observe that Q is close to one up to errors of about 5% for small energies. When the energy is close to the resonant energy of the double barrier, it is expected that Q is very close to 1 and this precisely what is shown in the figure. For higher energies, the approximation naturally breaks down since only the first resonant state has been taken into account and thus Q tends to zero. We have also represented the quantity $\|\varphi_p - \varphi_p^{\text{ext}}\|$ as a function of E, normalized such that $\max_E\|\varphi_p - \varphi_p^{\text{ext}}\| = 1$.

Table 4
Parameters for density computation

T	n_{d}^1	n_{d}^2	$k_{\max}$	N_{GR}	σ	$\Delta k_{\max}$	$\Delta k_{\min}$	N_{interp}
300 K	1×10^{24} m^{-3}	1×10^{21} m^{-3}	0.0626 Å^{-1}	3	0.0026 Å^{-1}	0.0008 Å^{-1}	0.0016 Å^{-1}	15

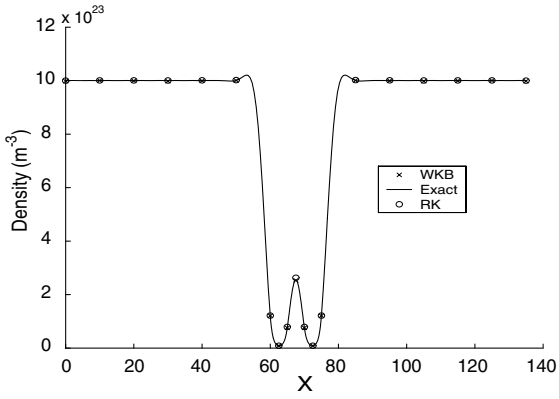

Fig. 14. Reference-WKB-RK density in the linear case.

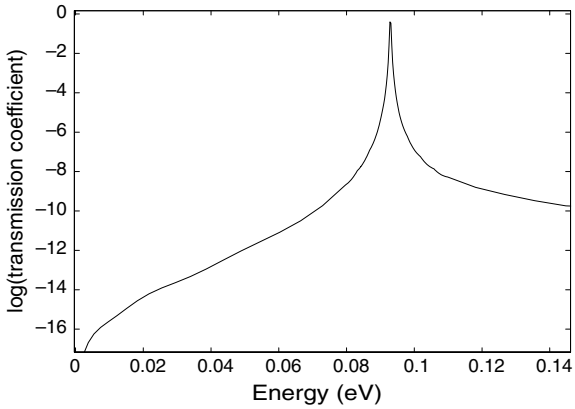

Fig. 15. Transmission coefficient for the linear case.

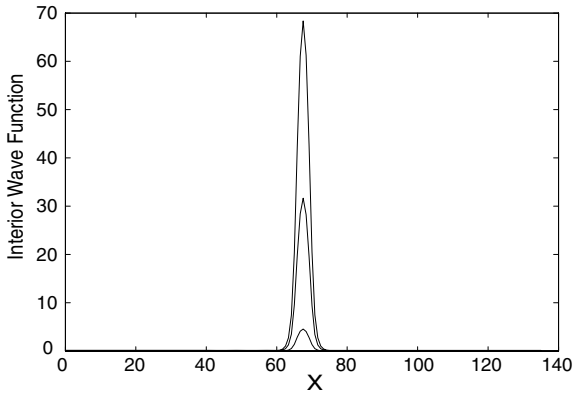

Fig. 16. Comparison of the interior wave function for different energies.

In the one-mode approximation, it is expected that $\varphi_p - \varphi_p^{\text{ext}} \approx \theta(p)e(x)$ only for the energies such that $\|\varphi_p - \varphi_p^{\text{ext}}\|$ is large (when $\|\varphi_p - \varphi_p^{\text{ext}}\|$ is small, this is a non-resonant case and thus $\varphi_p \approx \varphi_p^{\text{ext}}$). This is exacly what shows up in Fig. 17: the support of $\|\varphi_p - \varphi_p^{\text{ext}}\|$ is mainly localized in the region $Q \approx 1$.

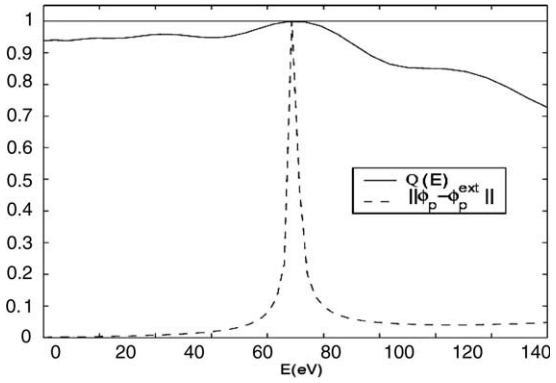

Fig. 17. Coefficient Q and normalized $\|\varphi_p - \varphi_p^{\text{ext}}\|$.

4.2.2. The fully non-linear problem

The self-consistent potential is computed thanks to the Gummel iterations [25], see [36] for more details. In order to compare precisely the methods, the mesh used for WKB being too coarse, the resolution of the Poisson equation is done on a refined (6 times finer here) grid with a linearly interpolated density between the WKB grid points. We took as a reference potential and density, the solution given by the method of [36] with an extremely refined mesh is chosen (1024). The results are shown in Figs. 18 and 19. The WKB grid has 34

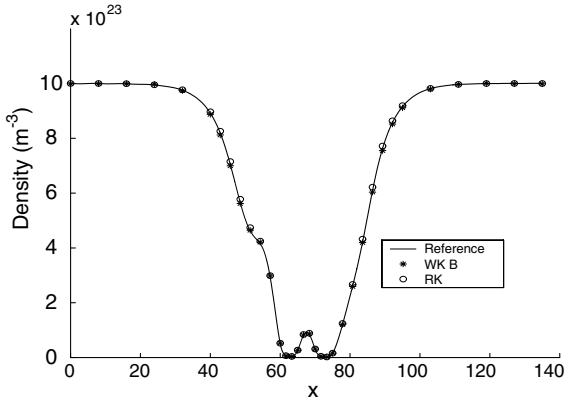

Fig. 18. Comparison Reference-WKB-RK: density for the fully non-linear case.

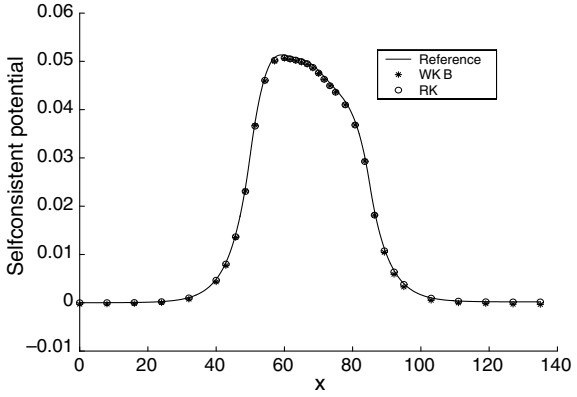

Fig. 19. Self-consistent potential for the fully non-linear case.

Table 5
Results for the fully non-linear problem

	Linear			Non-linear		
	N	Error	Time	N	Error	Time
WKB + one mode	19	0.0010	1	34	0.0030	1
RK + adaptative	232	0.0012	6	265	0.0040	5.5

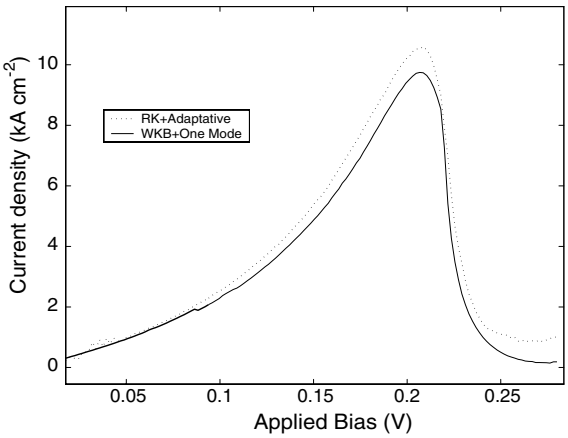

Fig. 20. Comparison of the I–V characteristics of a resonant tunneling diode.

points and the RK grid is 7 times finer. For almost the same error 0.3% and 0.4%, RK is about 5.5 times longer. The comparison of the methods is summarized in Table 5.

I–V characteristics. The current is computed thanks to (6). The obtained curves are shown in Fig. 20 and the combination of WKB-scheme and the one-mode approximation is about 5.4 faster than RK with the adaptative scheme. Notice that the curve obtained with the new method is under the one given by the method of [36] and is thus less accurate. At the peak location, there is discrepancy of about 10% between the two curves. The discrepancy between these curves relatively and the reference solution is of the same order of magnitude. Such differences can be explained by the fact that the current is a difference of two high quantities. Therefore, a small relative error on each of these high values may result in a bigger error on the difference. This is not the case for the density where the contributions add up instead of cancelling.

5. Conclusion

Two methods were introduced to accelerate the simulations of 1D stationary quantum transport in heterostructures. The numerical experiments showed the efficiency of the WKB-scheme and the Sjöstrand–Presilla one-mode approximation. The convergence analysis of the methods, in particular the unconditional convergence of the WKB method, is not performed in this paper and is postponed to a forthcoming work.

A natural extension concerns transient simulations. In the stationary picture, even using standard methods, the time cost is not that important since the structure is one-dimensional. In the time-dependent case, the simulation time is much more important because of two factors: the motion of the resonance when the applied bias changes and also the limitation to small time steps in order to avoid oscillations appearing at the boundaries. As long as the projection on the resonant modes is concerned, we would like to point out that the decomposition method due to Presilla and Sjöstrand and that we adapt here for numerical purposes is by no means restricted to the one-dimensional case. In two or three dimensions, potential applications are single electron memories which consist in quantum dots imbedded into barriers which exhibit the same feature as the double barrier. Here the number of resonances is potentially more than only one. Another potential application concerns the DG Mosfets with imbedded perpendicular oxide barriers in the channel. In this case, the

exterior wave functions have essentially a one-dimensional behaviour whereas the resonances are purely bidimensional. Further investigations on these topics are ongoing.

Acknowledgements

The authors acknowledge support from the HYKE project, contract number HPRN-CT-2002-00282, from the ACI Nouvelles Interfaces des Mathématiques No. ACINIM 176-2004 entitled "MOQUA" and funded by the French ministry of research. They thank the anonymous referees for their remarks on the manuscript.

Appendix A. Expressions of the coefficients of the WKB-scheme

We recall first that

$$\mathscr{I}_n = [x_n, x_{n+1}], \quad \mathscr{T} = \{x \in [a,b], E = V(x)\}.$$

We have

$$A_n = \begin{cases} \bullet & \text{if } \mathscr{I}_n \cap \mathscr{T} = \emptyset, \\ f_{n+1}(x_{n+\frac{1}{2}})\beta_n'(x_{n+\frac{1}{2}}) + f_{n+1}'(x_{n+\frac{1}{2}})\beta_n(x_{n+\frac{1}{2}}) + I_n(f_{n+1}\beta_n) & \text{if } |E - V(x)| > \delta, \\ \beta_n'(x_{n+\frac{1}{2}}) + I_n(\beta_n) & \text{if } |E - V(x)| < \delta, \\ \bullet & \text{if } \mathscr{I}_n \cap \mathscr{T} \neq \emptyset, \\ v_n'(x_{n+\frac{1}{2}}) + I_n(v_n) & \end{cases}$$

$$B_n = \begin{cases} \bullet & \text{if } \mathscr{I}_n \cap \mathscr{T} = \emptyset, \\ -f_n(x_{n+\frac{1}{2}})\alpha_n'(x_{n+\frac{1}{2}}) - f_n'(x_{n+\frac{1}{2}})\alpha_n(x_{n+\frac{1}{2}}) - I_n(f_n\alpha_n) & \text{if } |E - V(x)| > \delta, \\ -\alpha_n'(x_{n+\frac{1}{2}}) - I_n(\alpha_n) & \text{if } |E - V(x)| < \delta, \\ \bullet & \text{if } \mathscr{I}_n \cap \mathscr{T} \neq \emptyset, \\ -u_n'(x_{n+\frac{1}{2}}) - I_n(u_n) & \end{cases}$$

$$\tilde{B}_{n-1} = \begin{cases} \bullet & \text{if } \mathscr{I}_{n-1} \cap \mathscr{T} = \emptyset, \\ f_n(x_{n-\frac{1}{2}})\beta_{n-1}'(x_{n-\frac{1}{2}}) + f_n'(x_{n-\frac{1}{2}})\beta_{n-1}(x_{n-\frac{1}{2}}) - \tilde{I}_{n-1}(f_n\beta_{n-1}) & \text{if } |E - V(x)| > \delta, \\ \beta_n'(x_{n-\frac{1}{2}}) - \tilde{I}_{n-1}(\beta_n) & \text{if } |E - V(x)| < \delta, \\ \bullet & \text{if } \mathscr{I}_{n-1} \cap \mathscr{T} \neq \emptyset, \\ v_{n-1}'(x_{n-\frac{1}{2}}) - \tilde{I}_{n-1}(v_{n-1}) & \end{cases}$$

$$\tilde{C}_{n-1} = \begin{cases} \bullet & \text{if } \mathscr{I}_{n-1} \cap \mathscr{T} = \emptyset, \\ f_{n-1}(x_{n-\frac{1}{2}})\alpha_{n-1}'(x_{n-\frac{1}{2}}) + f_{n-1}'(x_{n-\frac{1}{2}})\alpha_{n-1}(x_{n-\frac{1}{2}}) - \tilde{I}_{n-1}(f_{n-1}\alpha_{n-1}) & \text{if } |E - V(x)| > \delta, \\ \alpha_n'(x_{n-\frac{1}{2}}) - \tilde{I}_{n-1}(\alpha_{n-1}) & \text{if } |E - V(x)| < \delta, \\ \bullet & \text{if } \mathscr{I}_{n-1} \cap \mathscr{T} \neq \emptyset, \\ u_{n-1}'(x_{n-\frac{1}{2}}) - \tilde{I}_{n-1}(u_{n-1}). & \end{cases}$$

where

$$I_n(g) = \frac{2m}{\hbar^2}\int_{x_n}^{x_{n+\frac{1}{2}}} (E - V(x))g(x)\,\mathrm{d}x, \quad \tilde{I}_{n-1}(g) = \frac{2m}{\hbar^2}\int_{x_{n-\frac{1}{2}}}^{x_n} (E - V(x))g(x)\,\mathrm{d}x.$$

The expressions of the derivative appearing in these formula are given by, for $x \in \mathscr{I}_n$,

$$\alpha_n'(x) = -\frac{\sqrt{2m}}{\hbar}\sqrt[+]{E - V(x)}\frac{\cos S_{n+1}(x)}{\sin \gamma_n},$$

$$\beta_n'(x) = \frac{\sqrt{2m}}{\hbar}\sqrt[+]{E - V(x)}\frac{\cos S_n(x)}{\sin \gamma_n},$$

$$f_n'(x) = \frac{V'(x)}{4}\frac{(E - V(x_n))^{1/4}}{(E - V(x))^{5/4}},$$

where

$$S_n(x) = \frac{\sqrt{2m}}{\hbar}\int_{x_n}^{x}\sqrt[+]{E - V(s)}\,\mathrm{d}s, \quad \gamma_n = \frac{\sqrt{2m}}{\hbar}\int_{x_n}^{x_{n+1}}\sqrt[+]{E - V(s)}\,\mathrm{d}s$$

Appendix B. Computation of the integrals I_n and $\tilde{I}_n$

B.1. Case V constant in $\mathscr{I}_n$

$$I_n(\alpha_n) = \frac{\sqrt{2m}}{\hbar \sin \gamma_n}\sqrt[+]{E - V}\left(\cos S_{n+1}(x_{n+\frac{1}{2}}) - \cos \gamma_n\right),$$

$$I_n(\beta_n) = \frac{\sqrt{2m}}{\hbar \sin \gamma_n}\sqrt[+]{E - V}\left(1 - \cos S_n(x_{n+\frac{1}{2}})\right),$$

$$\tilde{I}_n(\alpha_n) = \frac{\sqrt{2m}}{\hbar \sin \gamma_n}\sqrt[+]{E - V}\left(1 - \cos S_{n+1}(x_{n+\frac{1}{2}})\right),$$

$$\tilde{I}_n(\beta_n) = \frac{\sqrt{2m}}{\hbar \sin \gamma_n}\sqrt[+]{E - V}\left(\cos S_n(x_{n+\frac{1}{2}}) - \cos \gamma_n\right),$$

$$S_n(x) = \frac{\sqrt{2m}}{\hbar}\sqrt[+]{E - V}(x - x_n),$$

$$\gamma_n = \frac{\sqrt{2m}}{\hbar}\sqrt[+]{E - V}(x_{n+1} - x_n).$$

B.2. Case V non-constant in $\mathscr{I}_n$

The integrals $I_n(f_n\alpha_n), I_n(f_{n+1}\beta_n), \tilde{I}_n(f_n\alpha_n)$ and $\tilde{I}_n(f_{n+1}\beta_n)$ share all the same structure and consequently we will focus mainly on $I_n(f_{n+1}\beta_n)$. We have

$$I_n(f_{n+1}\beta_n) = \frac{2m(E - V(x_{n+1}))^{1/4}}{\hbar^2 \sin \gamma_n}\int_{x_n}^{x_{n+\frac{1}{2}}}(E - V(x))^{3/4}\sin S_n(x)\,\mathrm{d}x$$

which cannot be computed analytically. Thus, we make the following approximation, for any $x_n^0 \in \mathscr{I}_n$,

$$\begin{aligned}(E - V(x))^{3/4} &= \sqrt[+]{E - V(x)} \times (E - V(x))^{1/4} \\ &= \sqrt[+]{E - V(x)}(E - V(x_n^0))^{1/4}\left[1 + \mathcal{O}\left(\frac{V'(x_n^0)}{4(E - V(x_n^0))}(x_{n+1} - x_n)\right)\right]\end{aligned}$$

and then

$$I_n(f_{n+1}\beta_n) \approx \frac{2m(E-V(x_{n+1}))^{1/4}(E-V(x_n^0))^{1/4}}{\hbar^2 \sin\gamma_n}\int_{x_n}^{x_{n+\frac{1}{2}}} \sqrt[+]{E-V(x)}\sin S_n(x)\,\mathrm{d}x$$
$$\approx \frac{\sqrt{2m}(E-V(x_{n+1}))^{1/4}(E-V(x_n^0))^{1/4}}{\hbar \sin\gamma_n}\int_{S_n(x_n)}^{S_n(x_{n+\frac{1}{2}})} \sin S\,\mathrm{d}S$$
$$\approx \frac{\sqrt{2m}(E-V(x_{n+1}))^{1/4}(E-V(x_n^0))^{1/4}}{\hbar \sin\gamma_n}\left(\cos S_n(x_n) - \cos S_n(x_{n+\frac{1}{2}})\right),$$

where, if $V = a_n + b_n x$ in $\mathscr{I}_n$,

$$S_n(x) = \frac{\sqrt{2m}}{\hbar}\int_{x_n}^{x} \sqrt[+]{E-a_n-b_n s}\,\mathrm{d}s = \frac{2\sqrt{2m}}{3\hbar b_n}[(E-a_n-b_n x_n)^{3/2} - (E-a_n-b_n x)^{3/2}].$$

In the same way, we obtain

$$I_n(f_n\alpha_n) \approx \frac{\sqrt{2m}(E-V(x_n))^{1/4}(E-V(x_n^0))^{1/4}}{\hbar \sin\gamma_n}\left(\cos S_{n+1}\left(x_{n+\frac{1}{2}}\right) - \cos\gamma_n\right),$$
$$\tilde{I}_n(f_n\alpha_n) \approx \frac{\sqrt{2m}(E-V(x_n))^{1/4}(E-V(x_n^0))^{1/4}}{\hbar \sin\gamma_n}\left(1 - \cos S_{n+1}\left(x_{n+\frac{1}{2}}\right)\right),$$
$$\tilde{I}_n(f_{n+1}\beta_n) \approx \frac{\sqrt{2m}(E-V(x_{n+1}))^{1/4}(E-V(x_n^0))^{1/4}}{\hbar \sin\gamma_n}\left(\cos S_n\left(x_{n+\frac{1}{2}}\right) - \cos\gamma_n\right).$$

The expressions of $I_n(u_n)$ and $I_n(v_n)$ are easily calculated since the integrands are polynomials. One obtains

$$I_n(v_n) = \frac{2m}{\hbar^2}\left[b_n\left(\frac{x_n}{2}\left(x_{n+\frac{1}{2}}^2 - x_n^2\right) - \frac{1}{3}\left(x_{n+\frac{1}{2}}^3 - x_n^3\right)\right) + \frac{E-a_n}{2}\left(x_{n+\frac{1}{2}} - x_n\right)^2\right] \Big/ (x_{n+1}-x_n),$$
$$I_n(u_n) = \frac{2m}{\hbar^2}\left[(E-a_n)(x_{n+1}-x_n) - \frac{b_n}{2}\left(x_{n+\frac{1}{2}}^2 - x_n^2\right)\right] - I_n(v_n).$$

In the same manner, for $\tilde{I}_{n-1}(u_{n-1})$ and $\tilde{I}_{n-1}(v_{n-1})$, we have

$$\tilde{I}_{n-1}(v_{n-1}) = \frac{2m}{\hbar^2}\left[b_{n-1}\left(\frac{x_{n-1}}{2}\left(x_n^2 - x_{n-\frac{1}{2}}^2\right) - \frac{1}{3}\left(x_n^3 - x_{n-\frac{1}{2}}^3\right)\right)\right.$$
$$\left. + \frac{E-a_{n-1}}{2}\left((x_n - x_{n-1})^2 - \left(x_{n-\frac{1}{2}} - x_{n-1}\right)^2\right)\right] \Big/ (x_n - x_{n-1}),$$
$$\tilde{I}_{n-1}(u_{n-1}) = (E-a_{n-1})(x_n - x_{n-\frac{1}{2}}) - \frac{b_{n-1}}{2}\left(x_{n-1}^2 - x_{n-\frac{1}{2}}^2\right) - \tilde{I}_{n-1}(v_{n-1}).$$

References

[1] Y. Ando, T. Itoh, Calculation of transmission tunneling current across arbitrary potential barriers, J. Appl. Phys. 61 (4) (1986) 1479–1502.

[2] T. Abboud, J.-C. Nédélec, B. Zhou, Improvement of the integral equation method for high frequency problems, Mathematical and Numerical Aspects of Wave Propagation, SIAM, Philadelphia, 1995, pp. 178–187.

[3] X. Antoine, C. Besse, Construction, structure and asymptotic approximations of a microdifferential transparent boundary condition for the linear Schrödinger equation, J. Math. Pures Appl. (9) 80 (7) (2001) 701–738.

[4] A. Arnold, M. Ehrhardt, I. Sofronov, Discrete transparent boundary conditions for the Schrödinger equation, Rev. Matematica Univ. Parma 4 (2001) 57–108.

[5] A. Arnold, Mathematical concepts of open quantum boundary conditions, Trans. Theory Stat. Phys. 30 (2001) 561–584.

[6] J. Aguilar, J.M. Combes, A class of analytic perturbations for one-body Schrödinger Hamiltonians, Commun. Math. Phys. 22 (1971) 269–279.

[7] W. Bao, D. Jaksch, P.-A. Markowich, Numerical solution of the Gross–Pitaevskii equation for Bose–Einstein condensation, J. Comput. Phys. 187 (1) (2003) 318–342.

[8] W. Bao, S. Jin, P.-A. Markowich, On time-splitting spectral approximations for the Schrödinger equation in the semiclassical regime, J. Comput. Phys. 175 (2) (2002) 487–524.
[9] M. Baro, N. Ben Abdallah, P. Degond, A. El Ayyadi, A 1D coupled Schrödinger drift-diffusion model including collisions, J. Comput. Phys. 203 (1) (2005) 129–153.
[10] V.A. Baskakov, A.V. Popov, Implementation of transparent boundaries for numerical solution of the Schrödinger equation, Wave Motion 14 (1991) 123–128.
[11] N. Ben Abdallah, A hybrid kinetic-quantum model for stationary electron transport, J. Stat. Phys. 90 (3–4) (1998) 627–662.
[12] N. Ben Abdallah, On a multidimensional Schrödinger–Poisson scattering scattering model for semiconductors, J. Math. Phys. 41 (7) (2000) 4241–4261.
[13] N. Ben Abdallah, P. Degond, I. Gamba, Coupling one-dimensional time-dependent classical and quantum transport models, J. Math. Phys. 43 (1) (2002) 1–24.
[14] N. Ben Abdallah, P. Degond, P.-A. Markowich, On a one-dimensional Schrödinger–Poisson scattering model, Z. Angew. Math. Phys. 48 (1) (1997) 135–155.
[15] N. Ben Abdallah, C. Negulescu, M. Mouis, E. Polizzi, Simulation schemes for 2D nanoscale Mosfets, a WKB based method, J. Comput. Electron. (in press).
[16] D. Bohm, Quantum Theory, Dover, New York, 1989.
[17] M. Büttiker, Four-terminal phase-coherent conductance, Phys. Rev. Lett. 57 (1986) 1761–1769.
[18] S. Datta, Electronic Transport in Mesoscopic Conductors, Cambridge University Press, Cambridge, 1995.
[19] S. Datta, M.J. Mc Lennan, Quantum transport in ultrasmall electronic devices, Rep. Prog. Phys. 53 (1990) 1003–1114.
[20] P. Degond, A. El Ayyadi, A coupled Schrödinger drift-diffusion model for quantum semiconductor device simulations, J. Comput. Phys. 181 (1) (2002) 222–259.
[21] C. Fahrat, A. Macedo, M. Lesionne, A two-level domain decomposition method for the iterative solution of high frequency exterior Helmholtz problems, Numer. Math. 85 (2) (2000) 283–308.
[22] D.K. Ferry, S.M. Goodnick, Transport in Nanostructures, Cambridge University Press, Cambridge, 1997.
[23] B. Flannery, W. Press, S. Teukolsky, W. Vetterling, Numerical Recipes, Academic Press, New York, 1988.
[24] W.R. Frensley, Boundary conditions for open quantum driven far from equilibrium, Rev. Mod. Phys 62 (1990) 1570–1590.
[25] H.K. Gummel, A self-consistent iterative scheme for one-dimensional steady state transistor calculations, IEEE Trans. Electron. Devices ED-11 (1964) 455–465.
[26] G. Jona-Lasinio, C. Presilla, J. Sjöstrand, On Schrödinger equations with concentrated nonlinearities, Ann. Phys. 240 (1995) 1–21.
[27] R. Landauer, Electrical resistance of disordered one-dimensional lattices, Philos. Mag. 21 (1970) 863–876.
[28] C. Lent, D. Kirkner, The quantum transmitting boundary method, J. Appl. Phys. 67 (10) (1990) 6353–6359.
[29] S.E. Laux, A. Kumar, M. Fischetti, Analysis of quantum ballistic electron transport in ultrasmall silicon devices including space-charge and geometric effects, J. Appl. Phys. 95 (10) (2004) 5545–5582.
[30] P. Lochak, About the adiabatic stability of resonant states, Ann. Inst. Henri Poincaré A 39 (1983) 119–143.
[31] F. Nier, Schrödinger–Poisson systems in dimension $d \leqslant 3$: the whole-space case, Proc. Roy. Soc. Edinburgh A 123 (6) (1993) 1179–1201.
[32] F. Nier, A variational formulation of Schrödinger–Poisson systems in dimension $d \leqslant 3$, Commun. Partial Diff. Equ. 18 (7-8) (1993) 1125–1147.
[33] F. Nier, The dynamics of some quantum open systems with short-range nonlinearities, Nonlinearity 11 (4) (1998) 1127–1172.
[34] F. Nier, M. Patel, Nonlinear asymptotics for quantum out of equilibrium 1D systems: reduced models and algorithms, Conference "Multiscale methods in quantum mechanics, theory and experiments, Accademia dei Lincei Roma dec. 2002 (see http://name.math.univ-rennes1.fr/francis.nier/recherche/liste.html).
[35] M. Patel, Développement de modèles macroscopiques pour des systèques quantiques non linéaires hors équilibre, Ph.D. Thesis, Univ. Rennes, 2005, p. 1.
[36] O. Pinaud, Transient simulations of a resonant tunneling diode, J. Appl. Phys. 92 (4) (2002) 1987–1994.
[37] E. Polizzi, N. Ben Abdallah, Self-consistent three-dimensional models for quantum ballistic transport in open systems, Phys. Rev. B 66 (2002) 245301.
[38] E. Polizzi, N. Ben Abdallah, Subband decomposition approach for the simulation of quantum electron transport in nanostructures, J. Comput. Phys. 202 (1) (2005) 150–180.
[39] E. Polizzi, N. Ben Abdallah, O. Vanbésien, D. Lippens, Space lateral transfer and negative differential conductance regimes in quantum waveguide junctions, J. Appl. Phys. 87 (2000) 8700.
[40] C. Presilla, J. Sjöstrand, Transport properties in resonant tunneling heterostructures, J. Math. Phys. 37 (10) (1996) 4816–4844.
[41] B. Ricco, M.Y. Azbel, Physics of resonant tunneling, the one-dimensional barrier case, Phys. Rev. B. 29 (4) (1984) 1970–1976.
[42] A. Svizhenko, M.P. Anantram, T.R. Govindan, B. Biegel, R. Venugopal, Two-dimensional quantum mechanical modeling of nanotransistors, J. Appl. Phys. 91 (2002) 2343.
[43] R. Tsu, L. Esaki, Tunneling in a finite superlattice, Appl. Phys. Lett. 22 (1973) 562–564.
[44] R. Venugopal, Z. Ren, S. Datta, M.S. Lundstrom, D. Jovanovic, Simulating quantum transport in nanoscale transistors: real versus mode-space approaches, J. Appl. Phys. 92 (2002) 3730.
[45] B. Vinter, C. Weisbuch, Quantum Semiconductor Structures, Academic Press, New York, 1991.